Materials Horizons

ROYAL SOCIETY OF CHEMISTRY

COMMUNICATION

View Article Online
View Journal | View Issue

Published on 02 April 2021. Downloaded by East China Normal University on 7/6/2021 2:34:28 AM.

Cite this: *Mater. Horiz.*, 2021, 8, 1985

Received 6th January 2021,
Accepted 1st April 2021

DOI: 10.1039/d1mh00024a

rsc.li/materials-horizons

Flexo-photoelectronic effect in n-type/p-type two-dimensional semiconductors and a deriving light-stimulated artificial synapse†

Xiang Wang,[a] Xin Zhou,[a] Anyang Cui,*[a] Menghan Deng,[a] Xionghu Xu,[a] Liping Xu,[a] Yan Ye,[a] Kai Jiang,[a] Liyan Shang,[a] Liangqing Zhu,[a] Jinzhong Zhang,[a] Yawei Li,[a] Zhigao Hu*[abc] and Junhao Chu[abc]

Flexoelectricity and photoelectricity with their coupled effect (the so-called flexo-photoelectronic effect), are of increasing interest in the study of electronics and optoelectronics in van der Waals layered semiconductors. However, the related device design is severely restricted owing to the ambiguous underlying physical nature of flexo-photoelectronic effects originating from the co-manipulation of light and strain-gradients. Here, flexoelectric polarization and the flexo-photoelectronic effect of few-layered semiconductors have been multi-dimensionally investigated from high-resolution microscopic characterization on the nanoscale, physics analysis, and deriving a device design. We found that two back-to-back built-in electric fields form in bent InSe and WSe_2, and greatly modulate the transport behaviors of photogenerated carriers, further facilitating the separation of photogenerated electron–hole pairs and trapping the holes/electrons in InSe or WSe_2 channels, recorded in realtime by a home-made technique of lighting Kelvin probe force microscopy (KPFM). The slow release of trapped carriers contributes to the photoconductance relaxation after illumination. Utilizing the photoconductance relaxation, a light-stimulated artificial synapse based on the flexo-photoelectronic effect of bent InSe has been achieved. Significantly, all the pair-pulse facilitation (PPF) behavior, spike frequency-dependent excitatory post-synaptic current (EPSC) and the transition from short-term memory (STM) to long-term memory (LTM) have been successfully realized in this artificial synapse. This work adds to the investigation of flexo-photoelectronic effects on 2D optoelectronics, and moves towards the development of 2D neuromorphic electronics.

New concepts

The work firstly demonstrates the direct and systematic experimental evidence at the nanoscale, of the coupling between flexoelectric and photoelectric effects, originating from co-manipulation of light and strain-gradients. The novel flexo-photoelectronic effect of both bent n-type and p-type 2D semiconductors has been visualized *in situ* by the home-made lighting Kelvin probe force microscopy system. In addition, we provide a new strategy to manipulate photogenerated charges through the flexoelectric polarization potential in bent 2D semiconductors. Utilizing this strategy, a novel light-stimulated artificial synapse has been realized. The present results provide a ground-breaking and clear study on the flexo-photoelectronic effect of functional 2D materials, and derive an artificial synaptic device. It enhances the understanding of flexo-photoelectronic effects on 2D optoelectronics and serves in the future development of novel 2D flexible devices.

Wearability and flexibility are important targets for the next generation of electronic devices in order to satisfy the increasing demands of human–computer interactions and the portability of intelligent electronic devices.[1,2] As one of the promising candidates, two-dimensional (2D) layered semiconductors have attracted extensive attention in flexible electronics,[3–6] optoelectronics[7–10] and piezotronics[11–13] due to their excellent electrical transport, photoelectric and piezoelectric response, as well as the natural properties of being ultra-thin, flexible and transparent. For flexible devices, the properties of 2D materials are inevitably regulated by strain (stress).[14,15] Thus, it is valuable and significant to explore the property variation and the underlying strain-modulated mechanism of 2D materials under the stress field. Recently, the

[a] Technical Center for Multifunctional Magneto-Optical Spectroscopy (Shanghai), Engineering Research Center of Nanophotonics Advanced Instrument (Ministry of Education), Department of Materials, School of Physics and Electronic Science, East China Normal University, Shanghai 200241, China. E-mail: aycui@phy.ecnu.edu.cn, zghu@ee.ecnu.edu.cn; Fax: +86-21-54342933; Tel: +86-21-54345150

[b] Collaborative Innovation Center of Extreme Optics, Shanxi University, Taiyuan, Shanxi 030006, China

[c] Shanghai Institute of Intelligent Electronics and Systems, Fudan University, Shanghai 200433, China

† Electronic supplementary information (ESI) available: Basic optical and SEM images of few-layered InSe flakes suspended on the channel-patterned substrates; flexoelectric polarization and flexo-photoelectronic effect of bent WSe_2 minimal-layers; EPSC characterization and long-term memory behavior of light-stimulated artificial synapse. See DOI: 10.1039/d1mh00024a

Published on 02 April 2021. Downloaded by East China Normal University on 7/6/2021 2:34:28 AM.

strain engineering of 2D electronic and optoelectronic devices has been widely reported,[16–21] which brings new opportunities for fundamental physics and potential applications, along with new challenges. Most of the current research attributes the strain modulation of electric and photoelectric performances of 2D devices to bandgap modulation[16–18] or piezoelectric polarization,[19–21] but ignore the flexoelectric effect. We recently demonstrated that considerable flexoelectric polarization can be induced by strain-gradient in bent atomically thin MoS_2 and InSe.[22] Moreover, the locally conductive modification induced by flexoelectricity mainly focuses on some bulk semiconductors,[23–25] whereas the impact of flexoelectricity on the electronic and optoelectronics of 2D materials remains largely unexplored.

Compared with the bulk, the easily-deformed 2D layered semiconductor has a more prominent flexoelectric effect[26,27,28] which varies from the piezoelectric effect, because the latter only exists in a non-centrosymmetric direction but flexoelectricity is possible along any direction with strain-gradient.[29,30] Hence, 2D materials are considered to be an ideal system for probing flexoelectric effects. The microscopic characterization technique, such as scanning probe microscopy, is useful to observe flexoelectric polarization on 2D layered semiconductors.[31,32] Although the modulation of flexoelectric effects on electronic properties and performance plays a key role in almost all layered flexible devices, this issue still takes little attention at the device level owing to the technical and theoretical restrictions. Additionally, the coupling mechanism of flexoelectricity and photoelectric effect, the so-called flexo-photoelectronic effect, in the layered semiconductor based optoelectronic devices is still regarded as a crucial challenge before their practical electronic application.

In this study, we have systematically illustrated the flexo-photoelectronic coupling in bent few-layered InSe and WSe_2 films *via* piezoresponse force microscopy (PFM) and Kelvin probe force microscopy (KPFM). The flexoelectric polarization at the bent region could be clearly visualized through mapping and quantifying the measured effective out-of-plane piezoelectric coefficient (d_{33}^{eff}). The localization of charges induced by inhomogeneous strain in bent semiconductors is basically associated with the fluctuation of surface potential. Under illumination, the surface potential is gradually flattened by the redistribution of photogenerated carriers, where this potential kinetic process has been first observed in real-time on the nanoscale by a home-made lighting-KPFM test system. Back-to-back built-in electric fields induced by flexoelectric polarization contribute to the photogenerated holes/electrons trapped in bent n-type InSe (p-type WSe_2), resulting in photoconductance relaxation. Based on these fundamental observations, we successfully design a new light-stimulated synaptic device, in which the biologic synapse behaviors of short-term memory (STM), long-term memory (LTM), and spike frequency-dependent excitatory post-synaptic current (EPSC) could be commendably emulated at device level. Our results clearly reveal the flexo-photoelectronic effect of 2D layered semiconductors, from microscopic characterization to the design of light-stimulated synaptic devices. This work could pave the way to understand

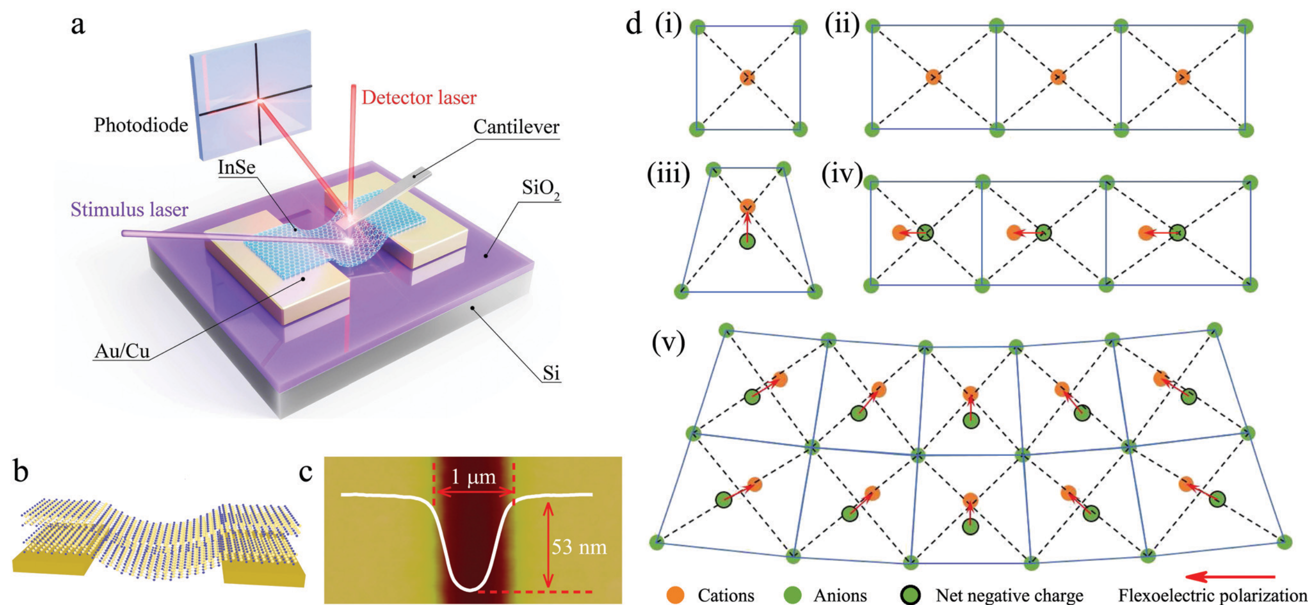

Fig. 1 Schematics of the experimental configuration and the basic mechanism of the flexoelectric effect. (a) Experimental schematic of PFM and lighting-KPFM system on the bent InSe device structure. (b) The ball-and-stick model and (c) the measured surface morphology of suspended InSe film between the two gold electrodes. The plotted curve shows the line profile topography perpendicular to the channel. (d) The flexoelectric effect of the well-defined centrosymmetric 2D semiconductor. (i) Unstrained lattice without net dipole under the case of the coincident electropositive and electronegative centers. (ii) Uniformly strained lattice. Net dipole moment is still zero because the centres of positive and negative charges are not changed. (iii) Inhomogeneously strained unit cell. Separated electropositive and electronegative centers yield a dipole moment. (iv) Homogeneously deformed on a whole, but the varied extent of deformation from cell to cell. Electropositive and electronegative centers misalign contributing to an uncompensated dipole moment. (v) In bent 2D semiconductor, both types of flexoelectric effects (iii and v) could coexist and induce a sum of flexoelectric polarization.

 This journal is © The Royal Society of Chemistry 2021

Published on 02 April 2021. Downloaded by East China Normal University on 7/6/2021 2:34:28 AM.

the inhomogeneous strain effects in 2D flexible devices, and also provide a valuable opportunity for designing 2D electronic neuromorphic devices.

Experimental configuration and flexoelectric polarization

Experimental schematic of PFM and lighting-KPFM based on scanning probe microscopy (SPM), and the structure representation diagram of the bent 2D InSe device, are shown in Fig. 1a. *In situ* measurement of the flexoelectric polarization and the evolution of the surface potential under the varied light field can be achieved synchronously by an SPM probe. A ball-and-stick model schematic and the measured surface morphology of 2D InSe suspended between two electrodes are illustrated in Fig. 1b and c, respectively. The inset plotted in Fig. 1c quantifies the line profile of topography along the direction perpendicular to the channel, showing the natural-suspended shape of InSe channel with a width of about 1 μm and the bent depth of approximately 53 nm. Optical images and scanning electron microscopy (SEM) images (Fig. S1 in ESI†) also demonstrate the bent deformation of the high quality suspended film. To elucidate flexoelectric coupling in the 2D semiconductor under non-uniform strain, Fig. 1d depicts the inverse flexoelectric effect of the well-defined centrosymmetric layer. The net dipole moment is zero in the unstrained centrosymmetric structure and is also maintained under the uniform strain, due to the coinciding center of positive and negative charges. When the unit cell is subjected to inhomogeneous deformation, the opposite shifts of electropositive and electronegative centers produces a net dipole moment.[33] Another case is the extent the deformation varies from cell to cell, despite the homogeneous deformation in each cell, where the cations shift off centre of the unit cell, then induce an uncompensated dipole moment.[30] In terms of the bent 2D film, the above-mentioned two types of flexoelectric effect commonly present simultaneously, inducing flexoelectric polarization along the radial direction and tangential direction, respectively.

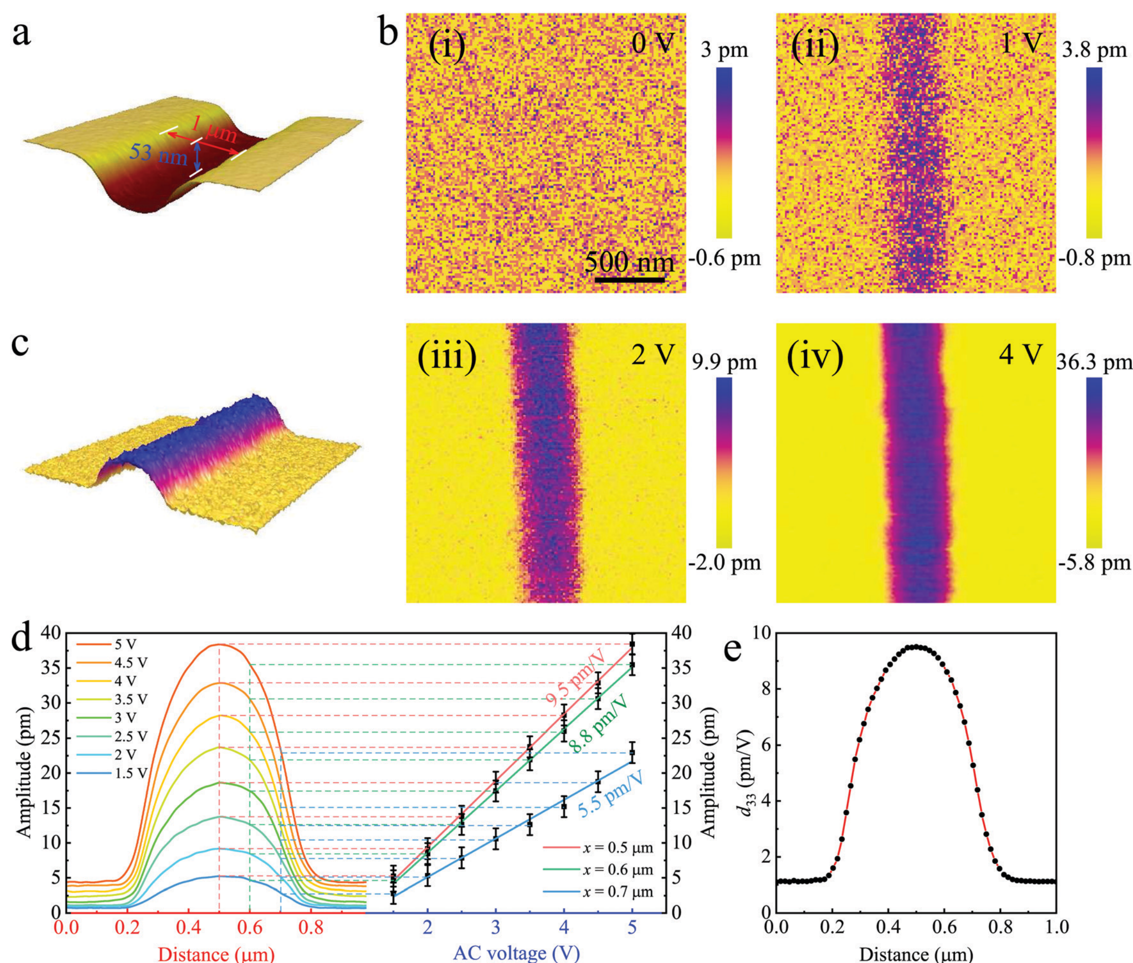

Fig. 2 The PFM measurements of the bent InSe-based device. (a) 3D AFM topography of the channel of the bent 2D InSe device. (b) Out-of-plane PFM amplitude images of suspended InSe channel under the ascending drive voltage of (i) 0 V, (ii) 1 V, (iii) 2 V, and (iv) 4 V, respectively. (c) 3D presentation of PFM amplitude map of suspended InSe channel under the drive voltage of 4 V. (d) Statistical distribution of PFM amplitude under the ascending drive voltage from 1.5 V to 5 V is plotted on the left side. The PFM amplitude response is plotted as the function *versus* the amplitude of drive voltage on the right side. Error bars signify the standard deviations of the d_{33}^{eff} coefficient mapped in 256 scan lines. (e) The distribution of the measured d_{33}^{eff} coefficient.

Published on 02 April 2021. Downloaded by East China Normal University on 7/6/2021 2:34:28 AM.

Static flexoelectric polarization considered as an analogue of piezoelectric polarization could be quantified by PFM technique,[22,32] and the results from the InSe device as a representative are illustrated in Fig. 2. The thickness of the InSe flake is about 11 nm. A flake thickness of 10–12 nm is controlled in our work, because it is widely proven to be an appropriate range for enhancing the electronic performance.[34,35] As shown in Fig. 2a, the suspended InSe deforms into the shape of a trench with a homogeneous and undamaged quality. Note that the polarization characterized by PFM is associated with the vector projection of flexoelectric polarization along the out-of-plane direction. PFM tests have been carried out on the suspended InSe channel under different drive voltages, $V_{AC} = V_{DC} + V_0\cos(\omega t)$ ($V_{DC} = 0$ in this work). Fig. 2b(i)–(iv) exhibit PFM amplitude images with the ascending drive voltage of V_0 magnitude from 0 to 5 V at a step size of 0.5 V. Apparently, the amplitude response at the bent region gradually increases with the drive voltage, while almost no amplitude value is achieved at the flat region. Amplitude signal derives from the flexoelectricity induced by the strain gradient rather than the intrinsic piezoelectric effect of InSe; this conclusion has also been verified by our previous work.[22] A 3D representation of the amplitude signal map measured at a drive voltage of 4 V in Fig. 2c shows that the polarization response gradually declines from the center of the channel to double edges, corresponding to the symmetric distribution of out-of-plane flexoelectric polarization.

In order to quantify the effective out-of-plane piezoelectric coefficient (d_{33}^{eff}) of bent InSe, the statistical distribution of PFM amplitude signals has been plotted mathematically on the left side of Fig. 2d. The d_{33}^{eff} coefficient can be calculated from the slope of the linear fitting curve, as shown on the right side of Fig. 2d, according to the equation:[36] $d_{33}^{\text{eff}} = \dfrac{A_P(\text{pm})}{V_0(\text{V})}$, where A_P is the driven piezoresponse displacement and V_0 is the amplitude of the applied alternating current (AC) drive voltage. The maximum value of the d_{33}^{eff} coefficient obtained at the center of the channel is about 9.5 pm V^{-1}, which greatly exceeds its intrinsic in-plane piezoelectric coefficient (d_{11} = 1.98 pm V^{-1}).[37] The findings indicate that the d_{33}^{eff} coefficient of bent 2D InSe dominantly comes from the flexoelectric effect rather than its intrinsic in-plane piezoelectricity. A more detailed analysis can be obtained in Note S1 and Fig. S2 of the ESI.† As can be seen from Fig. 2e, the d_{33}^{eff} coefficient almost symmetrically decreases on both sides of the channel, indicating that the flexoelectric polarization is also almost symmetrically distributed on the bent InSe flake. Similar findings and conclusions have also been found in the WSe_2-based device (Note S2 and Fig. S3 in the ESI†). The maximum d_{33}^{eff} coefficient in the center of the WSe_2 channel is about 4.9 pm V^{-1}, which is larger than its intrinsic in-plane piezoelectric coefficient (d_{11} = 2.79 pm V^{-1}).[38] These results confirm the strong flexoelectricity induced by the strain gradient in 2D semiconductor materials. Simultaneously, high-resolution spatial distribution of flexoelectric polarization in the suspended 2D devices has been firstly observed by the PFM method in the present work.

Coupling of flexoelectric effect and photoelectric effect

Redistribution of the charge concentration in 2D semiconductor flakes can result in variation of surface potential, when the flexoelectric polarization is yielded.[23] Moreover, the movement behavior of photogenerated charge carriers can be regulated by the flexoelectric polarization potential.[39] In order to observe the coupling of flexoelectricity and the photoelectric effect, we carried out *in situ* imaging of the surface potential evolution on a InSe device as the representative under 405 nm-laser illumination using a home-made lighting-KPFM setup, as presented in Fig. 3. In principle, surface potential from the KPFM method is directly measured as the contact potential difference (CPD) between the tip and sample.[40] In our experiment, the voltage is applied to the tip. Under this circumstance, the contact potential difference (V_{CDP}) can be expressed as $V_{CDP} = \dfrac{\phi_{\text{tip}} - \phi_{\text{sample}}}{e}$, where ϕ_{tip} is the work function of the tip, ϕ_{sample} is the work function of the sample, and e is the elementary charge. Thus, the lower surface potential means the higher work function is due to the same work function as the tip. As shown in Fig. 3a, without illumination, the surface potential at the channel (bent InSe) area is significantly lower than that at the double sides (flat InSe), leading to a potential well. With increasing light intensity, the surface potential of the bent area observably increases and finally exceeds that of the flat area, as shown in Fig. 3b–h. Simultaneously, the surface potential increases gradually overall with the light intensity, which could be attributed to the increase of photogenerated charge carriers.[41]

Under different illumination, the surface potential distribution along the direction perpendicular to the channel is plotted in Fig. 3i. In the case of the dark field, the surface potential is approximately horizontal on both sides, and dramatically drops off near the center. As a result, the surface potential of the center is more than 1000 mV lower than the edges, *i.e.*, the work function of the center is more than 1000 meV larger than that of the edges, hence, the energy band is bent.[42] As illustrated in Fig. 3i, with increasing light intensity, the difference of surface potential between bent and flat areas decreases gradually until the potential at the bent area exceeds that of the flat area, which might be related to the designated allocation of photo-induced charge carriers owing to the bent energy band. The same test has also been performed in a representative WSe_2 device, and in-depth information can be found in Fig. S4 in the ESI.† In the dark, the surface potential of the channel (bent WSe_2) is higher than that of the two sides (flat WSe_2) to establish a potential barrier. With increasing laser power intensity, the barrier decreases gradually until a potential well forms. In comparison to the observation of the bent InSe system, the contrary experimental results could be associated with the different nature of carrier: commonly InSe is an n-type semiconductor whereas WSe_2 is a p-type. The evolution of surface potential might be the related to the redistribution of photogenerated electrons and holes under the action of built-in electric fields, which is induced by flexoelectricity and might be different in n-type and p-type semiconductors.

 This journal is © The Royal Society of Chemistry 2021

Published on 02 April 2021. Downloaded by East China Normal University on 7/6/2021 2:34:28 AM.

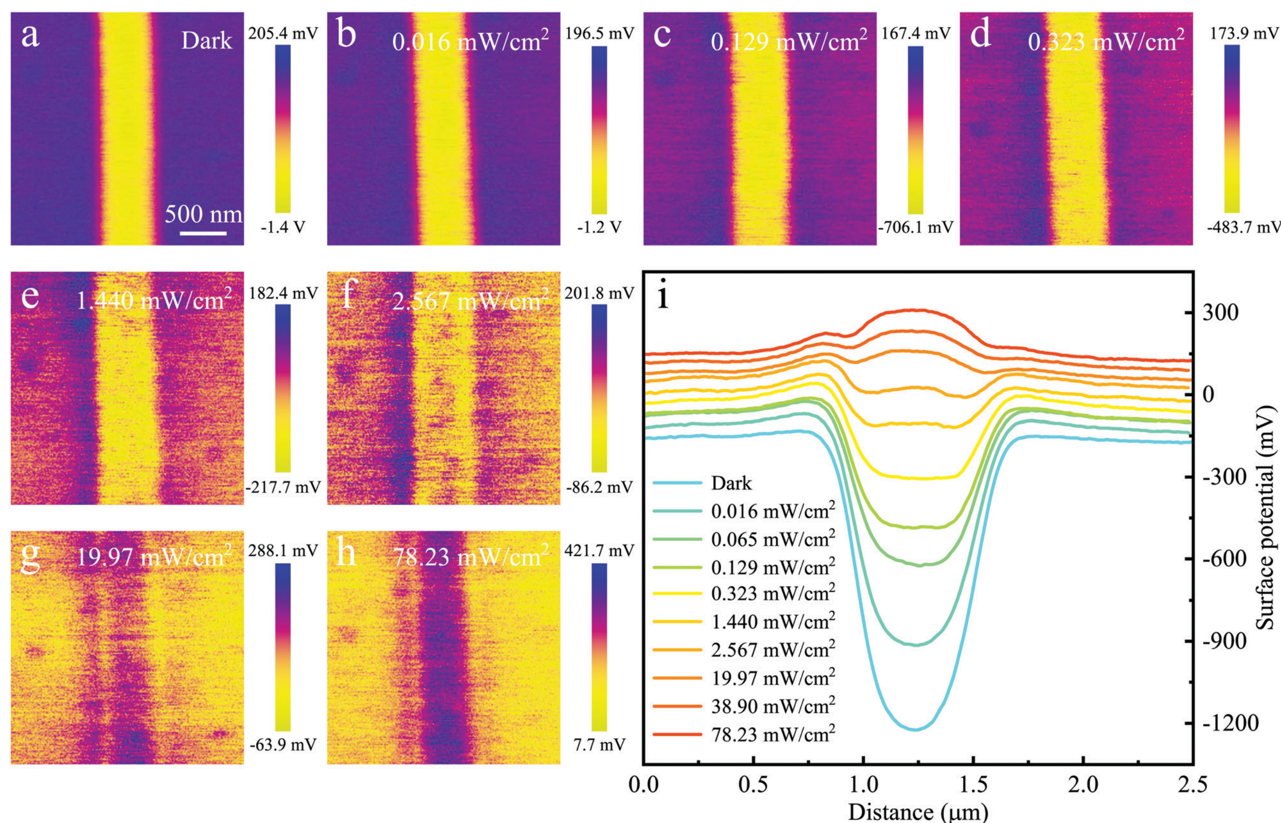

Fig. 3 The lighting-KPFM measurements of the bent InSe-based device. The surface potential images of bent InSe channel under (a) the dark and under the 405 nm laser with an intensity of (b) 0.016 mW cm^{-2}, (c) 0.129 mW cm^{-2}, (d) 0.323 mW cm^{-2}, (e) 1.440 mW cm^{-2}, (f) 2.567 mW cm^{-2}, (g) 19.97 mW cm^{-2} and (h) 78.23 mW cm^{-2}. (i) The surface potential distribution along the direction perpendicular to the channel under different illumination.

Furthermore, to investigate the channel-width dependence of flexoelectricity in 2D devices, the thin-layered InSe was transferred upon the prefabricated substrates with three kinds of grooves (Fig. S1 in the ESI†). Then the surface topography, PFM and KPFM measurements were carried out, as shown in Fig. 4. Obviously, the bending depth, PFM amplitude response and the surface potential contrast all enhance with increasing the channel-width. The crucial parameters and data are listed in Fig. 4. As summarized in Fig. 4, the same InSe flake on the tailor-made substrate with three channels, deforms with depths of 24 nm, 30 nm, and 57 nm, corresponding to the three kinds of channel widths of 0.75 μm, 1.06 μm and 1.58 μm, respectively. It is noted that the wider channel could create a greater strain-gradient, leading to the stronger flexoelectric effect. Both the corresponding d_{33}^{eff} coefficient and difference of surface potential (ΔV_{CPD}) in Fig. 4 reflect the positive correlation dependence between flexoelectricity and channel-width. The results indicate that the flexoelectric effect of 2D materials could be easily modulated through changing the naturally bent shape of film manipulated by the supporting substrate.

We further demonstrate the flexo-photoelectric effect from the coupling of the flexoelectric and photoelectric effects. For clarity, Fig. 5 shows the energy band diagrams presenting the underlying physical mechanisms of the flexo-photoelectric effect. In the pristine n-type InSe flake, the charge carriers uniformly distribute corresponding to a flat band structure. While in the suspended 2D InSe, the charge localization induced by the inhomogeneous strain makes the energy band bend.[16] Apparently, the charge redistribution in the 2D semiconductor takes place as the flexoelectric polarization is generating. The net negative charges accumulate at the middle area, forming depletion zones on both sides,[43] resulting in the upwards bending of the band structure at the middle, as shown in Fig. 5b. Thus, the work function of the middle region is larger than that of both sides, in good accordance with KPFM results of the InSe device in the dark field.

More importantly, the built-in electric fields at the two sides both point toward the middle area. As a consequence, under laser illumination, the photogenerated electron–hole pairs are split apart by the built-in electric fields.[21] Correspondingly, the holes are trapped in the potential well, while the electrons are pushed to the two side areas, as depicted in Fig. 5c. As the trapped holes accumulate in the bent InSe, the surface potential difference between the bent and flat regions gradually decreases, leading to the bit by bit flattening of the bent band, until the back-to-back built-in electric fields are fully compensated.[16,24] The transport behavior of the photogenerated electron and hole in the 2D InSe device has been proved by the clear evolution of surface potential under laser irradiation. As shown in Fig. 3i, the enhancement of surface potential of

View Article Online

Published on 02 April 2021. Downloaded by East China Normal University on 7/6/2021 2:34:28 AM.

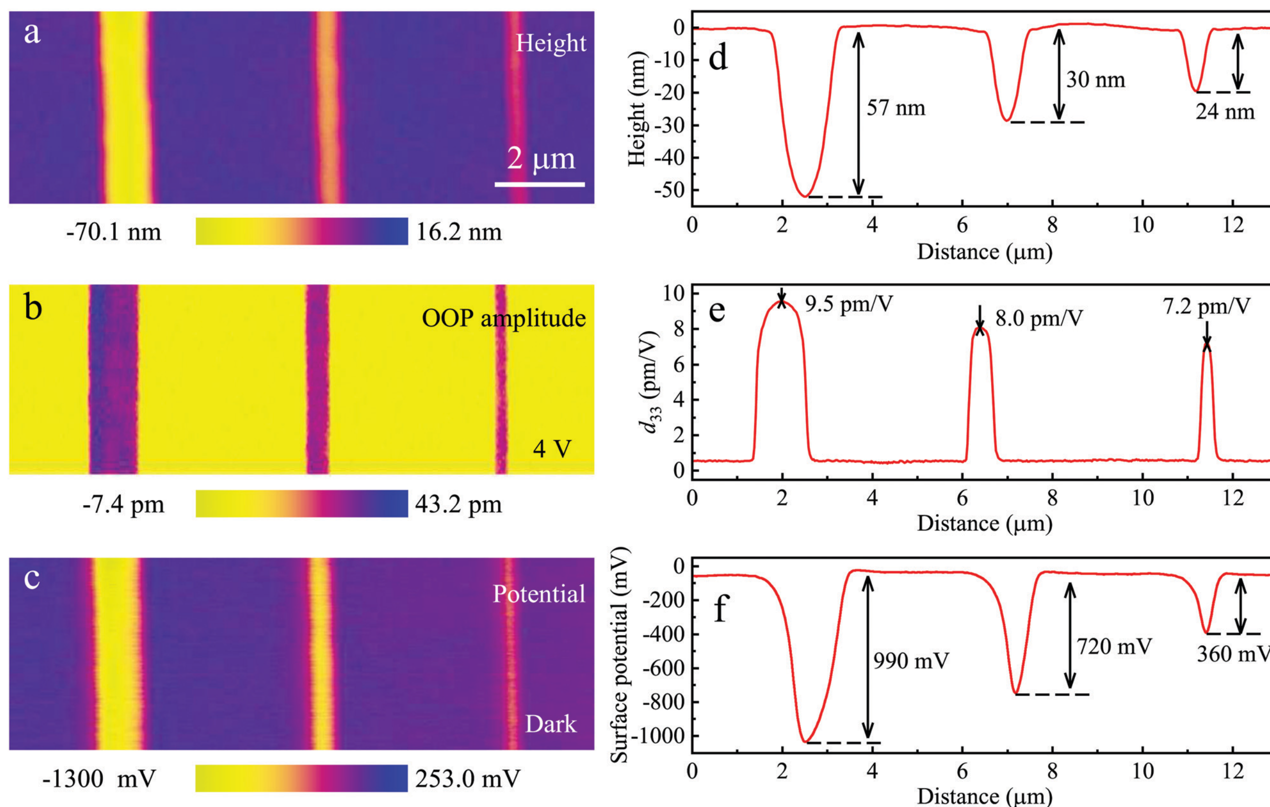

Fig. 4 Channel-width-dependent flexoelectricity in bent InSe with few-layers. (a) Surface morphology, (b) out-of-plane (OOP) amplitude mapping under the drive voltage of 4 V, and (c) surface potential mapping of InSe flakes suspended on three channels with widths of 0.75 μm, 1.06 μm and 1.58 μm. The statistical distribution of (d) surface morphology, (e) d_{33}^{eff} coefficient and (f) surface potential along the direction perpendicular to the channels.

the bent region gradually slows down with increasing light intensity, indicating the limited hole-trapping capacity of the bent InSe channel. Note that in Fig. 3i, the surface potential of suspended InSe eventually slightly exceeds that of supported

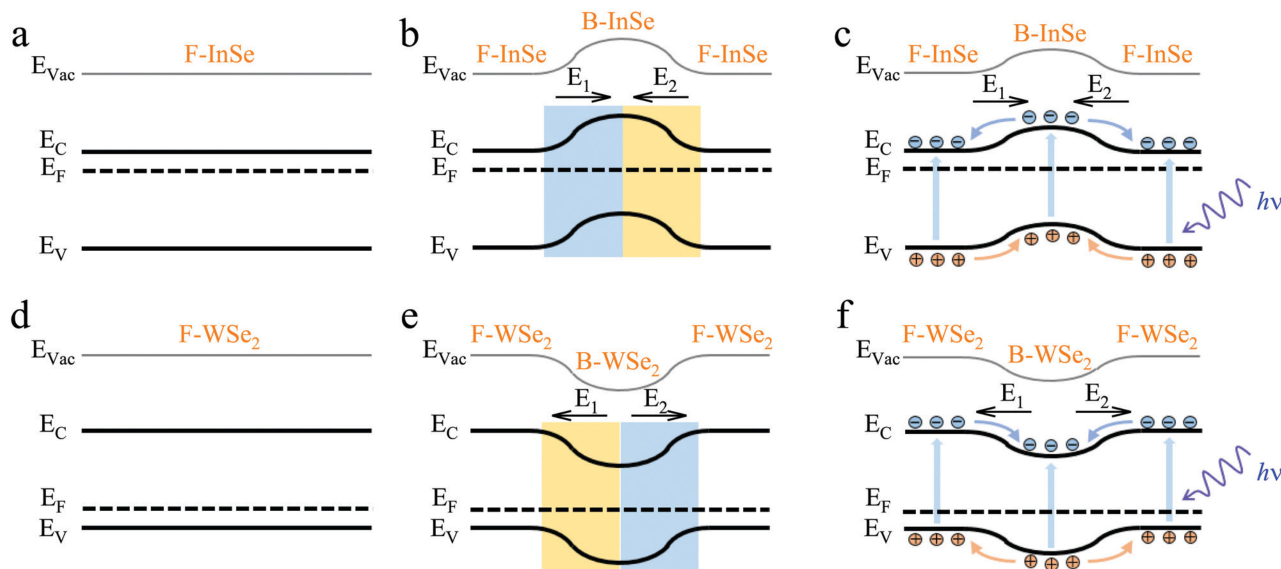

Fig. 5 The mechanism analysis of the coupling behavior of the flexoelectric effect and photoelectric effect. Energy band structures of (a) flat InSe (F-InSe) and (b) bent InSe (B-InSe). (c) Energy band structure and the transport behavior of photogenerated charge carriers in bent InSe device under light illumination. Energy band structures of (d) flat WSe_2 (F-WSe_2) and (e) bent WSe_2 (B-WSe_2). (f) Energy band structure and transport behavior of photogenerated charge carriers in the bent WSe_2 device under light illumination.

This journal is © The Royal Society of Chemistry 2021

Published on 02 April 2021. Downloaded by East China Normal University on 7/6/2021 2:34:28 AM.

InSe when the light intensity is greater than 2.567 mW cm^{-2}. The anomalous result could be attributed to the metal–semiconductor interface band-structure engineering,[23] which leads to the work function of the few-layered InSe supported by gold electrodes increasing, while that of suspended InSe is not affected.[44] Once Au and InSe are in contact, electrons will flow into the Au layer from the InSe layer. At equilibrium, the Fermi levels align to form the Schottky barrier, resulting in upward bending of the InSe energy band.[45] As a result, the work function of InSe supported by Au is higher than that of the suspended one, inducing the contact potential difference collected by KPFM at the flat region to be lower than the one collected at the bent region.

Conversely, in p-type WSe_2, the energy band bends downwards in the middle owing to the accumulating of net positive charges at the center region, as presented in Fig. 5e, forming the back-to-back built-in electric fields. When the photogenerated electron–holes are yielded (see Fig. 5f), the electrons would be trapped in the middle, and the holes move to the two sides. The opposite energy band structures of bent InSe and WSe_2 are responsible for the inverse of the KPFM results as mentioned above. Similarly, with strong light intensity, the surface potential of suspended WSe_2 is slightly lower than the supported one, causing the downward bending of WSe_2 energy bands near the interface with Au.[23,44]

Light-stimulated artificial synapse based on the flexo-photoelectronic effect

Today, the rapid development of artificial intelligence techniques and smart robots urgently demands advanced multifunctional optoelectronic devices that can satisfy the self-adaptive detecting, processing, and memorizing of optical information. However, conventional photodetectors are generally passive and non-tunable, making it technically difficult to handle data-intensive tasks and meet the requirements of real-time information processing and storage.[46] Towards the future development of superior and smart optoelectronic devices, light-stimulated synaptic devices have become one of the promising candidates. The synaptic devices can not only directly respond to the optical signals, but also perform temporary memory and real-time processing of optical information and sensory data through sensing information in ways like biological nervous systems with light-tunable and time-dependent plasticity.[47] Additionally, in the big data and post-Moore's law era, we must fundamentally change the modern computing way based on the von Neumann architecture to break through the so-called von Neumann bottleneck. Artificial neural networks (Ann), a data-centric computing method, is considered as a promising alternative. Synapses are the basic functional components that enable information flow, data processing and memory in the human brain.[48] Therefore, the realization of electronic devices with synaptic functions is a crucial step in the future development of neural network computers.

We indicate that photoelectric performance of bent 2D semiconductors could be greatly modified through the back-to-back built-in electric fields induced by the flexoelectric effect. The opposite built-in electric fields could not only facilitate the separation of carriers, but also store electrons or holes, preventing them from recombination with holes or electrons.[49,50] Owing to the efficient separation of carriers, the response rate of photocurrent speeds up.[39] Besides, photoconduction after illumination maintains and decreases very slowly, owing to the gradual release process of trapped carriers.[51,52] The delayed decay of photocurrent is crucial to light-stimulated devices with a memory function.[53–55] The rapid photoresponse and photocurrent memory effect are regarded as the significant factors for realizing light-stimulated synaptic performance.

Here, we first design light-stimulated synaptic devices based on the flexo-photoelectronic effect of the layered semiconductors. Fig. 6a shows the schematic diagram of a biological synapse, which is the functional link between the neurons. In Fig. 6b, a structural illustration of the artificial synapse indicates that the few-layered InSe flake is suspended on the gold electrodes at both sides. The flat InSe directly contacts with the electrodes, while the bent InSe acts as the channel, whose width and depth are about 1 μm and 50 nm, respectively. The thickness of the InSe flake is about 11 nm. The 300 nm SiO_2 layer at the bottom plays a role in supporting the electrodes and insulation. Additional details of device structure can be obtained from the optical and SEM images (Fig. S1 in the ESI†). The basic I–V curves of the representative InSe device in the dark and under continuous illumination, are displayed in Fig. S5 of the ESI.† The I–V curves under various irradiation intensity are all symmetric and linear, which is consistent with the symmetric structure of the device. As two key figures of merit of the photoelectric device, responsivity (R_{ph}) and detectivity (D^*) can be extracted from the I–V curves. At the fixed bias of 0.1 V, the maximum values of R_{ph} and D^* of our bent-InSe devices can reach up to 288.7 A W^{-1} and 2.45×10^{12} Jones, respectively, which are slightly better than previously reported results (with R_{ph} = 157 A W^{-1} and $D^* \sim 10^{11}$ Jones) in traditional InSe phototransistors.[56] The details about the calculation method of R_{ph} and D^* can be obtained in Note S3 of the ESI.†

The typical excitatory post-synaptic current (EPSC) of our light-stimulated synaptic devices is shown in Fig. S6a in the ESI.† Applying a light spike (405 nm, 38.9 mW cm^{-2}, 200 ms), the EPSC rapidly rises and reaches a maximum value at the end of the light spike at about 4.1 nA. Subsequently, the EPSC gradually declines back to the initial current owing to the slow release of trapped holes at the InSe channel. In psychology, memory retention is commonly characterized using the stretched exponential function (SEF),[57,58] which can be expressed as:[55] $I = (I_0 - I_\infty)\cdot\exp\left[-\left(\frac{t-t_0}{\tau}\right)^\alpha\right] + I_\infty$, where I_0 and I_∞ are the EPSC value at the end of the light spike and the final post-synaptic current value, respectively, τ and t_0 are the feature relaxation time and light spike finish time, and α is an index between 0 and 1. The observed EPSC decay of our

Published on 02 April 2021. Downloaded by East China Normal University on 7/6/2021 2:34:28 AM.

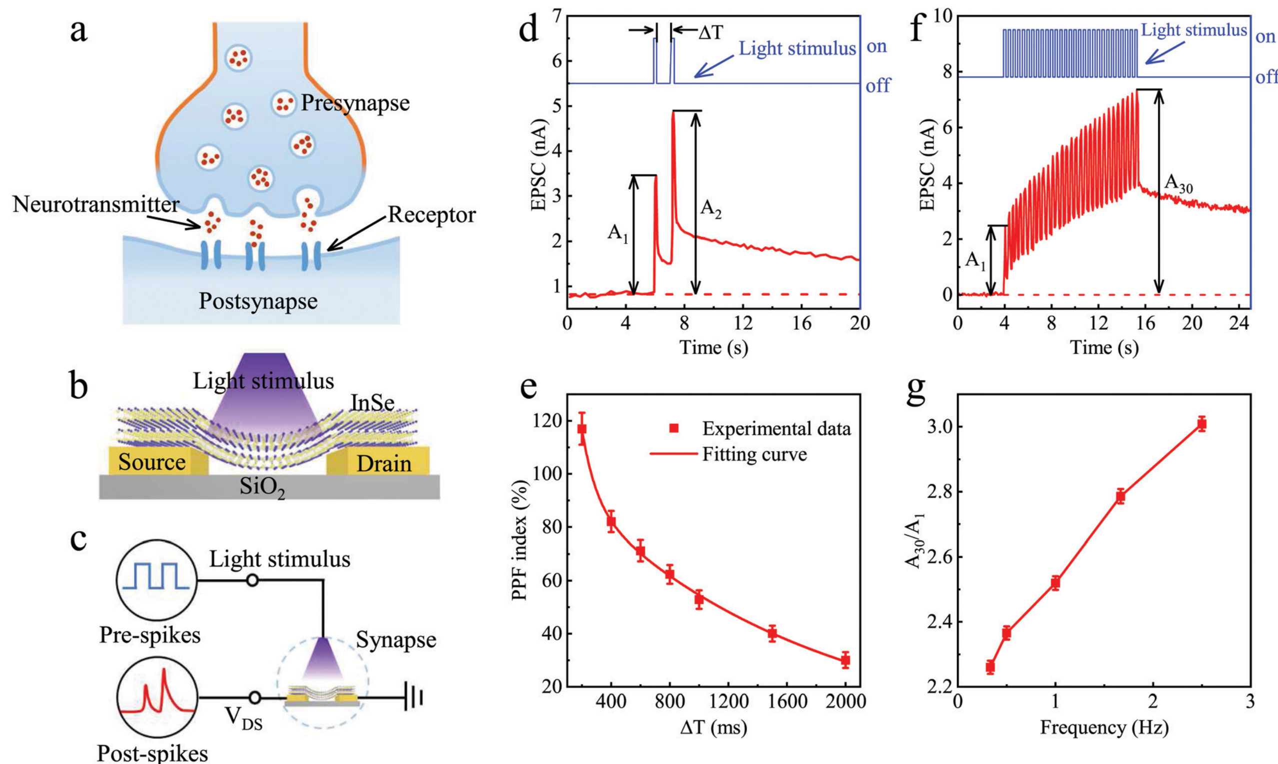

Fig. 6 The simulation of PPF behavior and high-pass filtering function. (a) The schematic diagram of a biological synapse. (b) The structure illustration of the light-stimulated artificial synaptic device. (c) The schematic of PPF measurement. (d) EPSC triggered by a pair of light spikes (405 nm, 38.9 mW cm^{-2}, 200 ms) with a fixed reading bias of 0.1 V. A_1 and A_2 are the values of the EPSC peaks at the end of the first and second light spike, respectively. (e) The interval time dependence of the PPF index. The power density of the laser and each pulse width are fixed at 38.9 mW cm^{-2} and 200 ms, respectively. (f) EPSC triggered by thirty consecutive light spikes with a fixed reading bias of 0.1 V. A_1 and A_{30} are the values of the EPSC peaks at the end of the first and thirtieth light spike, respectively. (g) The frequency dependence of EPSC gain (A_{30}/A_1). The power density of laser and pulse width are fixed at 38.9 mW cm^{-2} and 200 ms, respectively, we only change the interval time to change the frequency. Error bars represent standard errors from three repeats of independent experiments.

artificial synapses can be fitted well with the SEF (Fig. S6b in ESI†), indicating the similarity with biological synapses. To investigate the light-field modulation on EPSC behavior, the pulse width-dependent EPSC change is illustrated in Fig. S6c in the ESI.† As the pulse width increases from 1 ms to 1000 ms, the EPSC change increases dramatically at the beginning, and then levels off. The similar variation tendency of EPSC change also appears with increasing light pulse intensity (Fig. S6d in ESI†). The phenomena may be attributed to the limited hole-trapping capacity of the bent InSe channel. The findings indicate that the EPSC behavior of our artificial synapse can be efficiently modulated by a light-field.

In biology, the memory and learning behaviors of the nervous system can be defined as two categories: short-term memory (STM) and long-term memory (LTM). The STM process lasts from milliseconds to minutes, while the LTM remains for a few hours or more.[48] Generally, STM could transit to LTM *via* repetition training and rehearsal.[59] Pair-pulse facilitation (PPF),[60] as a typical STM behavior, described the EPSC enhancement after two sequential synaptic stimuli, which is considered as an important index for the artificial synaptic device. Fig. 6c clearly demonstrates the imitation of the PPF based bent-InSe synaptic device. As shown in Fig. 6d, the representative PPF behavior of our bent InSe device is triggered *via* the two sequential light spikes (405 nm, 38.9 mW cm^{-2}, 200 ms), whose interval time (ΔT) is 1000 ms. The bias applied to the source and drain is fixed at 0.1 V. Obviously, the second EPSC peak (A_2), which was triggered by the latter presynaptic spike, is larger than the first EPSC peak (A_1) triggered by the former spike. This phenomenon can be attributed to the increasing trapped charges after the two light spikes. If the interval time of two spikes is not enough for complete release of charges trapped during the first spike, the unreleased trapped charges would accumulate to the next spike, and so on. The PPF index can be expressed as[61] $\mathrm{PPF} = 100\% \times \dfrac{A_2 - A_1}{A_1}$, where A_1 and A_2 are the magnitudes of the first and second EPSC peaks, respectively. Furthermore, the interval time dependent PPF index is demonstrated in Fig. 6e. With decreasing interval time ΔT, the PPF index increases gradually and reaches the maximum value of 117% when ΔT is 200 ms. Biologically, the PPF decay contains both a slow phase and rapid phase, and can be mathematically demonstrated as[62] $\mathrm{PPF} = c_1 \cdot \exp\left(-\dfrac{\Delta T}{\tau_1}\right) + c_2 \cdot \exp\left(-\dfrac{\Delta T}{\tau_2}\right)$, where ΔT is the interval between light pulses, c_1 and c_2 represent the initial facilitation

This journal is © The Royal Society of Chemistry 2021

Published on 02 April 2021. Downloaded by East China Normal University on 7/6/2021 2:34:28 AM.

magnitudes of the rapid and slow phase, respectively, and τ_1 and τ_2 represent the featured relaxation times of the rapid and slow phase, respectively. It can be seen from the fitting curve in Fig. 6e that the PPF behavior mimicked by the light-stimulated 2D bent InSe synaptic device is in complete agreement with the double-exponential function. In our case, τ_1 and τ_2 are about 96 ms and 1626 ms, respectively, whose magnitudes are comparable to those of a biological synapse.[61]

In neuroscience, the synapse is a junction between neurons that allows presynaptic neurons to transmit signals to post-synaptic neurons, with the ability to change its efficacy in the short or long term.[48,63] The change induced by historical activity could be enhancement or depression, and the activity-dependent synaptic plasticity is considered to be responsible for memory and learning. In neural network communication, synapses play the role of dynamic filter for information processing of multiple biological signals.[48,63] As shown in Fig. 6f, the EPSC response increases gradually when applying successive light pulse stimulation, under the fixed reading voltage of 0.1 V. After the 30th spike, the EPSC value is defined as A_{30}, and the EPSC value after the first spike is A_1. A_{30} exceeds A_1 by three times, when the frequency of the presynaptic spikes (405 nm, 38.9 mW cm^{-2}, 200 ms) is 2.5 Hz. The spike frequency dependence of the EPSC gain (defined as A_{30}/A_1) is plotted in Fig. 6g. Apparently, the EPSC gain increases rapidly with the presynaptic spike frequency, indicating that the high-pass filtering characteristic of the neurons could be emulated using our artificial synapse. As is known, the defects in channel materials might also result in persistent photoconductivity. To examine the contribution of defects in our bent-InSe devices, the controlled experiments were carried out on the flat InSe devices. As depicted in Note S4 and Fig. S7 of the ESI,† the results of the controlled experiments indicate that the persistent photoconductivity of bent-InSe devices mainly comes from the contribution of the band bending induced by the flexoelectric effect rather than the contribution of the defect.

The human brain stores information through repetition and rehearsal.[64] Moreover, the brain memory level is usually up to the learning intensity and repetition frequency. Such synaptic plasticity also could be imitated in our designed artificial synapse, as shown in Fig. 7. Herein, the change of channel conductance is considered as the memory level. To study the learning and forgetting characteristics of the light-stimulated synapse, the normalized channel conductance changes ($\Delta G(t)/\Delta G_0$) are plotted as the function of time. Fig. 7a shows the declining behavior of the normalized channel conductance changes after applying 5, 10, 20, 30 and 50 presynaptic spikes. Simultaneously, Fig. 7b and c demonstrate the normalized channel conductance change decay under different power density and pulse width, respectively. The number of light stimuli can be deemed to be the number of learning times, meanwhile, the power density and pulse width of each spike can be regarded as learning intensity. Obviously, the decay rate of normalized channel conductance change decreases with increasing pulse number, power density or pulse width. These phenomena are highly consistent with learning processing in the brain.

In addition, after applying presynaptic spikes, the normalized channel conductance changes attenuated drastically at the

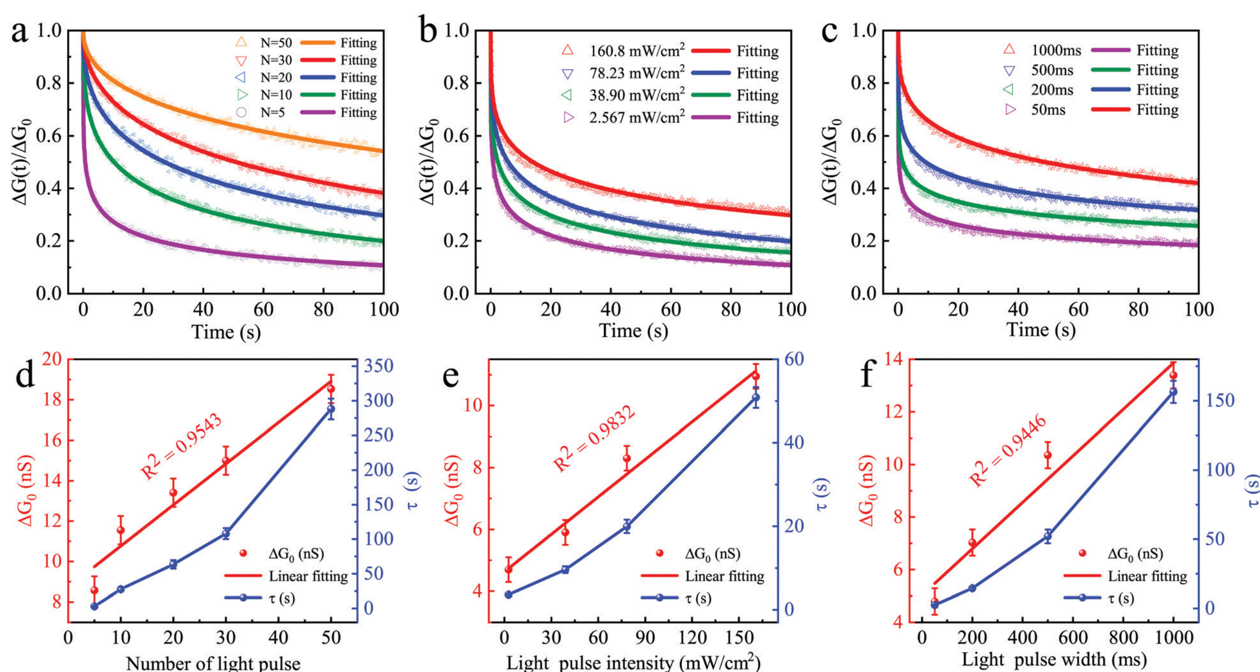

Fig. 7 The learning and forgetting characteristics of the artificial synaptic device. The normalized channel conductance change ($\Delta G(t)/\Delta G_0$) as a function of time with (a) different number of light pulses, (b) different power density of laser, and (c) different light pulse width. (d) Light pulse number-dependent, (e) laser power density-dependent, and (f) light pulse width-dependent channel conductance change (ΔG_0) and feature relaxation time (τ). The values of τ are obtained from the fitting curves. Error bars represent standard errors from three repeat independent experiments.

Published on 02 April 2021. Downloaded by East China Normal University on 7/6/2021 2:34:28 AM.

beginning and then decreased slowly, being analogous to the forgetting pattern of the human brain.[52,65] As shown in Fig. 7a–c, the decay behavior of the normalized channel conductance changes could be fitted by the well-known Ebbinghaus forgetting curve, which could be expressed as[66] $\Delta G(t)/\Delta G_0 = \exp\left[-\left(\frac{t}{\tau}\right)^{\beta}\right]$, where $\Delta G(t) = G(t) - G_{\text{initial}}$ and $\Delta G_0 = G_0 - G_{\text{initial}}$, $G(t)$ is the channel conductance at time t, G_0 is the channel conductance at the end of the last spike of light pulse, G_{initial} is the channel conductance before any external stimulus, τ is the feature relaxation time, and β is an index between 0 and 1. The corresponding channel conductance and feature relaxation time τ obtained from the fitting curves in Fig. 7a–c are presented in Fig. 7d–f, respectively. Both the channel conductance and relaxation time increased with the pulse number, power density or pulse width, indicating that the enhancement of impression and the reduction of forgetting could be achieved by increasing learning frequency or strengthening learning intensity. Moreover, the conductance variations show high-linearity with the pulse number, power density and pulse width with the R-square of 0.9543, 0.9832 and 0.9446, respectively. The results indicated that our bent InSe-based synaptic device could implement linear conductance change with the adjustment of presynaptic spikes. It is noteworthy that the relaxation time prolonged from 3.3 s to 288.1 s when the number of presynaptic spikes added was from 5 to 50, suggesting that the possibility of transition from short-term memory (STM) to long-term memory (LTM) is increased by the increase in repetitive training. Therefore, we applied 200 presynaptic spikes (405 nm, 38.9 mW cm^{-2}, 200 ms) with the interval time as 1000 ms in our artificial synapse to observe its LTM behaviors. As shown in Fig. S8 of the ESI,† at 40 000 seconds (11.1 h) after light stimulation, the EPSC still maintains at about 2.6 nA, which is over 1.5 times the resting current (about 1.7 nA), and the normalized channel conductance change is also retained at about 0.25. The simulation results indicate that our light-stimulated artificial synapse devices not only successfully reproduce the short-term plasticity of biological synapses, but also commendably realize the long-term plasticity.

Furthermore, energy consumption is very important for an artificial synapse. In terms of the human brain, the energy consumption is only 10–100 fJ per synaptic event.[67] Herein, the power consumption of our bent InSe-based synaptic devices is considered. The electrical and optical energy consumption (E_{ele} and E_{opt}) for a single event is defined as $E_{\text{ele}} = I_{\text{peak}} \times t \times V$, and $E_{\text{opt}} = P_{\text{in}} \times t \times A$, where I_{peak}, t, V, P_{in} and A are the peak value of the EPSC, the pulse duration time, the reading voltage, the laser irradiation intensity, and the effective area, respectively. At the fixed reading voltage of 0.1 V, for a presynaptic spike with the laser power of 38.9 mW cm^{-2} and the pulse duration time of 1 ms, our InSe-based artificial synapse can reach the ultralow electrical and optical energy consumption of about 100 fJ (with I_{peak} of about 1 nA) and 3.89 pJ, respectively. The optical energy consumption of our device could be further reduced by reducing the device dimensions.

Our high-performance bent-InSe-based light-stimulated synaptic device as a classical instance shows the great potential of flexo-photoelectronic effects in the design and application of optoelectronic devices and neural devices. Our artificial synaptic devices tactfully utilize the built-in back-to-back electric fields induced by flexoelectric polarization in bent InSe to obtain photoconductance relaxation, and further realize the simulation of synaptic behaviors. Specifically, the back-to-back electric fields are achieved by the opposite flexoelectric polarization induced by the almost symmetric strain distribution in the bent InSe channel. When the light stimulus is applied, photo-induced electron–hole pairs are generated and rapidly split apart by the back-to-back electric fields. Subsequently, the electrons participate in conduction, and holes are trapped in the center of the bent InSe channel. After the light stimulus is removed, the photoconductance will decline slowly due to the release of trapped holes. As a result, the basic synaptic behaviors could be gracefully imitated in the bent-InSe-based devices through manipulating the width, intensity and number of presynaptic light pulses.

In conclusion, we have carefully observed and quantified the distribution of flexoelectric polarization induced by the strain-gradient in the bent 2D InSe and WSe_2 on the nanoscale using a high-resolution PFM technique. The measured d_{33}^{eff} coefficients achieve maximum values of about 9.5 pm V^{-1} and 4.9 pm V^{-1} at the centers of bent InSe and WSe_2 channels, respectively, then decrease at both edges, indicating the gradient-distribution of flexoelectric polarization. The *in situ* KPFM system collects the redistribution of charge carriers induced by flexoelectric polarization in the bent InSe and WSe_2 flakes. Furthermore, the carrier concentration mapping on the bent InSe and WSe_2 by a self-built lighting KPFM reveals the transportation kinetics of photogenerated electrons and holes. The underlying physical nature of flexo-photoelectric coupling effects have been presented by elucidating the energy band structures. The findings indicate that the back-to-back built-in electric fields in the bent 2D semiconductors are established, facilitating the separation of photogenerated electron–hole pairs and trapping the electrons or holes to the center of channels. After illumination, the trapped charge carriers would be released slowly, resulting in the sustained photoconductance effect.

Taking advantage of the photoconductance relaxation effect, we have designed and successfully achieved a novel good-performance lighted-stimulated artificial synapse based on the bent 2D InSe device. The learning and forgetting characteristics of biological synapses, such as short-term plasticity, long-term plasticity and high-pass filtering, have been carefully simulated *via* our artificial synapse. This study would promote the development and understanding of the photoelectric, piezoelectric, flexoelectric effect and the coupled flexo-photoelectric effect of van der Waals layered materials and the deriving electronic devices, as well as paving a new path for 2D optoelectronic and neuromorphic devices.

Materials and methods

Device fabrication

The patterned substrates were fabricated on heavily n-doped silicon wafers with 300 nm SiO_2 by electron beam lithography

 This journal is © The Royal Society of Chemistry 2021

Published on 02 April 2021. Downloaded by East China Normal University on 7/6/2021 2:34:28 AM.

(EBL, Pioneer Two, Raith). After developing, 200 nm copper and 50 nm gold were thermally evaporated onto the top of SiO_2. Through the lift-off process, the Au/Cu electrodes were left behind and the channels with a depth of about 250 nm were formed. The widths of channels are set in the range between 0.5 μm and 2 μm. Then, the thin-layered γ-InSe and 2H-WSe_2 flakes, which were mechanically exfoliated from the single crystals of bulk γ-InSe and 2H-WSe_2, were transferred onto the electrodes with the help of scotch tape and polydimethylsiloxane (PDMS). After transfer, the thin-layered InSe and WSe_2 flakes were suspended between the electrodes, and the bending depth at the center of the channel is usually between 20 and 90 nm.

Characterization of surface morphology

The surface morphology and thickness of suspended thin-layered InSe and WSe_2 flakes were measured using a commercial atomic force microscope (AFM) system (Dimension Icon, Bruker). The surface morphology was also collected by scanning electron microscopy (SEM) based on the EBL (Pioneer Two, Raith) system.

Flexoelectric polarization mapping

All PFM measurements were carried out with the contact mode of the AFM system (Dimension Icon, Bruker). The conductive tip coated by Pt/Ir was employed with the tip radius of about 20 nm, a force constant around 2.8 N m^{-1}, resonant frequency of about 75 kHz. During the PFM measurements, the frequency of the applied AC drive signal is fixed at 15 kHz for avoiding contact resonance.

Surface potential mapping

All surface potential measurements were performed on a *Peak-Force* based KPFM system (Dimension Icon, Bruker) with the same conductive tip. The drive routing was set at the tip with the lift scan height of 60 nm. The lighting-KPFM test system was remoulded further. A commercial 405 nm laser was adopted, whose power density is tunable with the range from 0.016 mW cm^{-2} to 245.2 mW cm^{-2}. Note that the chosen laser wavelength (405 nm) is far from the wavelength of an extremely-weak laser (about 690 nm) in the AFM detector, avoiding additional influence on the measurements. The external laser was focused under the tip through the self-built light path during KPFM tests, and the diameter of the light beam is about 3 mm, which is much larger than the size of artificial synapse devices.

Artificial synapse device measurements

All electrical performances were measured at room temperature by a semiconductor parameter analyzer (4200-SCS, Keithley). For the characterization of light-stimulated synaptic functions, the same 405 nm laser adopted in the lighting-KPFM measurements was used as the light source.

Author contributions

X. Wang, A. Cui and Z. Hu initiated and designed the experiments and wrote the manuscript. X. Wang, M. Deng, X. Xu and Y. Ye gave discussions about KPFM and PFM data. X. Wang, X. Zhou and L. Xu conducted the experiments for device fabrication and electrical measurements. K. Jiang, J. Zhang, L. Zhu, L. Shang, Y. Li and J. Chu gave the detailed analyses of the underlying mechanism. All of the authors contributed to the manuscript preparation.

Conflicts of interest

There are no conflicts to declare.

Acknowledgements

This work was financially supported by the National Natural Science Foundation of China (Grants No. 91833303, 61974043, 61805081, and 61674057), the National Key Research and Development Program of China (Grants No. 2018YFB0406500, 2017YFA0303403, and 2019YFB2203400), Projects of Science and Technology Commission of Shanghai Municipality (Grant No. 18JC1412400, 18YF1407000, 18YF1407200, and 19511120100), China Postdoctoral Science Foundation (Grants No. 2020TQ0099, and 2020M681222), and the Program for the Professor of Special Appointment (Eastern Scholar) at the Shanghai Institutions of Higher Learning.

References

1 J. Kim, A. S. Campbell, B. E. de Ávila and J. Wang, *Nat. Biotechnol.*, 2019, **37**, 389–406.
2 B. Wang and A. Facchetti, *Adv. Mater.*, 2019, **31**, 1901408.
3 M. Choi, S. R. Bae, L. Hu, T. Hoang and J. H. Ahn, *Sci. Adv.*, 2020, **6**, eabb5898.
4 Q. Xue, J. F. Sun, Y. Huang, M. S. Zhu, Z. X. Pei, H. F. Li, Y. K. Wang, N. Li, H. Y. Zhang and C. Y. Zhi, *Small*, 2017, **13**, 1701827.
5 Z. Y. Lin, Y. Huang and X. F. Duan, *Nat. Electron.*, 2019, **2**, 378–388.
6 P. F. Jia, W. J. Chen, J. B. Qiao, M. Zhang, X. H. Zheng, Z. Y. Xue, R. D. Liang, C. S. Tian, L. He, Z. F. Di and X. Wang, *Nat. Commun.*, 2019, **10**, 3127.
7 Q. H. Wang, K. Kalantar-Zadeh, A. Kis, J. N. Coleman and M. S. Strano, *Nat. Nanotechnol.*, 2012, **7**, 699–712.
8 O. Lopez-Sanchez, D. Lembke, M. Kayci, A. Radenovic and A. Kis, *Nat. Nanotechnol.*, 2013, **8**, 497–501.
9 M. Long, P. Wang, H. Fang and W. Hu, *Adv. Funct. Mater.*, 2019, **29**, 1803807.
10 M. J. Dai, H. Y. Chen, F. K. Wang, Y. X. Hu, S. Wei, J. Zhang, Z. G. Wang, T. Y. Zhai and P. A. Hu, *ACS Nano*, 2019, **13**, 7291–7299.
11 J. H. Lee, J. Y. Park, E. B. Cho, T. Y. Kim, S. A. Han, T. H. Kim, Y. Liu, S. K. Kim, C. J. Roh, H. J. Yoon, H. Ryu, W. Seung, J. S. Lee, J. Lee and S. W. Kim, *Adv. Mater.*, 2017, **29**, 160667.
12 W. Z. Wu, L. Wang, Y. L. Li, F. Zhang, L. Lin, S. M. Niu, D. Chenet, X. Zhang, Y. F. Hao, T. F. Heinz, J. Hone and Z. L. Wang, *Nature*, 2014, **514**, 470–474.

Published on 02 April 2021. Downloaded by East China Normal University on 7/6/2021 2:34:28 AM.

13 L. Chen, Z. G. Yu, D. Liang, S. Li and K. W. Ang, *Nano Energy*, 2020, **76**, 105020.
14 D. Akinwande, N. Petrone and J. Hone, *Nat. Commun.*, 2014, **5**, 5678.
15 Z. H. Dai, L. Q. Liu and Z. Zhang, *Adv. Mater.*, 2019, **31**, 1805414.
16 X. H. Peng, Q. Wei and A. Copple, *Phys. Rev. B: Condens. Matter Mater. Phys.*, 2014, **90**, 085402.
17 S. Manzeli, A. Allain, A. Ghadimi and A. Kis, *Nano Lett.*, 2015, **15**, 5330–5335.
18 Z. Li, Y. Lv, L. Ren, J. Li, L. Kong, Y. Zeng, Q. Tao, R. Wu, H. Ma, B. Zhao, D. Wang, W. Dang, K. Chen, L. Liao, X. Duan, X. Duan and Y. Liu, *Nat. Commun.*, 2020, **11**, 1151.
19 H. Zhu, Y. Wang, J. Xiao, M. Liu, S. Xiong, Z. J. Wong, Z. Ye, Y. Ye, X. Yin and X. Zhang, *Nat. Nanotechnol.*, 2015, **10**, 151–155.
20 W. Z. Wu, W. Lei, R. M. Yu, Y. Y. Liu, S. H. Wei, J. Hone and Z. L. Wang, *Adv. Mater.*, 2016, **28**, 8463–8468.
21 P. Lin, L. P. Zhu, D. Li, L. Xu, C. F. Pan and Z. L. Wang, *Adv. Funct. Mater.*, 2018, **28**, 1802849.
22 X. Wang, A. Y. Cui, F. F. Chen, L. P. Xu, Z. G. Hu, K. Jiang, L. Y. Shang and J. H. Chu, *Small*, 2019, **15**, 1903106.
23 L. F. Wang, S. H. Liu, X. L. Feng, C. L. Zhang, L. P. Zhu, J. Y. Zhai, Y. Qin and Z. L. Wang, *Nat. Nanotechnol.*, 2020, **15**, 661.
24 M. M. Yang, A. N. Iqbal, J. J. P. Peters, A. M. Sanchez and M. Alexe, *Nat. Commun.*, 2019, **10**, 2791.
25 R. Guo, L. You, W. Lin, A. Abdelsamie, X. Shu, G. Zhou, S. Chen, L. Liu, X. Yan, J. Wang and J. Chen, *Nat. Commun.*, 2020, **11**, 2571.
26 S. Das, B. Wang, T. R. Paudel, S. M. Park, E. Y. Tsymbal, L. Q. Chen, D. Lee and T. W. Noh, *Nat. Commun.*, 2019, **10**, 537.
27 T. D. Nguyen, S. Mao, Y. W. Yeh, P. K. Purohit and M. C. McAlpine, *Adv. Mater.*, 2013, **25**, 946–974.
28 X. Y. Zhuang, B. He, B. Javvaji and H. S. Park, *Phys. Rev. B*, 2019, **99**, 054105.
29 A. Abdollahi, N. Domingo, I. Arias and G. Catalan, *Nat. Commun.*, 2019, **10**, 1266.
30 S. V. Kalinin and A. N. Morozovska, *Nat. Nanotechnol.*, 2015, **10**, 916.
31 S. Kang, S. Jeon, S. Kim, D. Seol, H. Yang, J. Lee and Y. Kim, *ACS Appl. Mater. Interfaces*, 2018, **10**, 27424–27431.
32 C. J. Brennan, R. Ghosh, K. Koul, S. K. Banerjee, N. Lu and E. T. Yu, *Nano Lett.*, 2017, **17**, 5464–5471.
33 R. Maranganti and P. Sharma, *Phys. Rev. B: Condens. Matter Mater. Phys.*, 2009, **80**, 054109.
34 M. Li, C. Lin, S. Yang, Y. Chang, J. Chang, F. Yang, C. Zhong, W. Jian, C. Lien, C. Ho, H. Liu, R. Huang, W. Li, Y. Lin and J. Chu, *Adv. Mater.*, 2018, **30**, 1803690.
35 M. Li, F. Yang, Y. Hsiao, C. Lin, H. Wu, S. Yang, H. Li, C. Lien, C. Ho, H. Liu, W. Li, Y. Lin and Y. Lai, *Adv. Funct. Mater.*, 2019, **29**, 1809119.
36 N. Syed, A. Zavabeti, J. Z. Ou, M. Mohiuddin, N. Pillai, B. J. Carey, B. Y. Zhang, R. S. Datta, A. Jannat, F. Haque, K. A. Messalea, C. Xu, S. P. Russo, C. F. McConville, T. Daeneke and K. Kalantar-Zadeh, *Nat. Commun.*, 2018, **9**, 3618.
37 Y. Guo, S. Zhou, Y. Z. Bai and J. J. Zhao, *Appl. Phys. Lett.*, 2017, **110**, 163102.
38 K. A. N. Duerloo, M. T. Ong and E. J. Reed, *Nano Energy*, 2012, **19**, 2871–2876.
39 J. Lu, J. Yao, J. Yan, W. Gao, L. Huang, Z. Zheng, M. Zhang and J. Li, *Mater. Horiz.*, 2020, **7**, 1427–1435.
40 A. M. Somoza and E. Palacios-Lidón, *Phys. Rev. B*, 2020, **101**, 075432.
41 J. Byeon, J. Kim, J. Kim, G. Lee, K. Bang, N. Ahn and M. Choi, *ACS Energy Lett.*, 2020, **5**, 2580–2589.
42 K. Zhang, T. Zhang, G. Cheng, T. Li, S. Wang, W. Wei, X. Zhou, W. Yu, Y. Sun, P. Wang, D. Zhang, C. Zeng, X. Wang, W. Hu, H. J. Fan, G. Shen, X. Chen, X. Duan, K. Chang and N. Dai, *ACS Nano*, 2016, **10**, 3852–3858.
43 B. Schuler, J. Lee, C. Kastl, K. A. Cochrane, C. T. Chen, S. Refaely-Abramson, S. Yuan, E. van Veen, R. Roldán, N. J. Borys, R. J. Koch, S. Aloni, A. M. Schwartzberg, D. F. Ogletree, J. B. Neaton and A. Weber-Bargioni, *ACS Nano*, 2019, **13**, 10520–10534.
44 A. Allain, J. Kang, K. Banerjee and A. Kis, *Nat. Mater.*, 2015, **14**, 591–595.
45 Y. Huang, Y. Chen, Y. Ho, S. Huang, Y. Chang, K. Watanabe, T. Taniguchi, H. Chiu, C. Liang, R. Sankar, F. Chou, C. Chen and W. Wang, *ACS Appl. Mater. Interfaces*, 2018, **10**, 33450–33456.
46 F. P. G. de Arquer, A. Armin, P. Meredith and E. H. Sargent, *Nat. Rev. Mater.*, 2017, **2**, 16100.
47 Z. Cheng, C. Ríos, W. H. Pernice, C. D. Wright and H. Bhaskaran, *Sci. Adv.*, 2017, **3**, e1700160.
48 L. F. Abbott and W. G. Regehr, *Nature*, 2004, **431**, 796–803.
49 M. Buscema, J. O. Island, D. J. Groenendijk, S. I. Blanter, G. A. Steele, H. S. J. van der Zanta and A. Castellanos-Gomez, *Chem. Soc. Rev.*, 2015, **44**, 3691–3718.
50 C. Xie, C. Mak, X. M. Tao and F. Yan, *Adv. Funct. Mater.*, 2017, **27**, 1603886.
51 Y. Wang, Z. Y. Lv, J. R. Chen, Z. P. Wang, Y. Zhou, L. Zhou, X. L. Chen and S. T. Han, *Adv. Mater.*, 2018, **30**, 1802883.
52 T. Chang, S. H. Jo and W. Lu, *ACS Nano*, 2011, **5**, 7669–7676.
53 K. Zhang, D. H. Meng, F. M. Bai, J. Y. Zhai and Z. L. Wang, *Adv. Funct. Mater.*, 2020, **30**, 2002945.
54 K. Wang, S. Dai, Y. Zhao, Y. Wang, C. Liu and J. Huang, *Small*, 2019, **15**, 1900010.
55 S. Dai, X. Wu, D. Liu, Y. Chu, K. Wang, B. Yang and J. Huang, *ACS Appl. Mater. Interfaces*, 2018, **10**, 21472–21480.
56 S. R. Tamalampudi, Y. Y. Lu, U. R. Kumar, R. Sankar, C. D. Liao, B. K. Moorthy, C. H. Cheng, F. C. Chou and Y. T. Chen, *Nano Lett.*, 2014, **14**, 2800–2806.
57 D. C. Rubin and A. E. Wenzel, *Psychol. Rev.*, 1996, **103**, 734–760.
58 W. A. Wickelgren, *J. Math. Psychol.*, 1972, **9**, 418–455.
59 J. L. McGaugh, *Science*, 2000, **287**, 248–251.
60 P. P. Atluri and W. G. Regehr, *J. Neurosci.*, 1996, **16**, 5661–5671.
61 R. S. Zucker and W. G. Regehr, *Annu. Rev. Physiol.*, 2002, **64**, 355–405.

 This journal is © The Royal Society of Chemistry 2021

62 Y. H. Liu, L. Q. Zhu, P. Feng, Y. Shi and Q. Wan, *Adv. Mater.*, 2015, **27**, 5599–5604.
63 E. S. Fortune and G. J. Rose, *Trends Neurosci.*, 2001, **24**, 381.
64 R. Lamprecht and J. LeDoux, *Nat. Rev. Neurosci.*, 2004, **5**, 45–54.
65 T. Ohno, T. Hasegawa, T. Tsuruoka, K. Terabe, J. K. Gimzewski and M. Aono, *Nat. Mater.*, 2011, **10**, 591–595.
66 S. G. Hu, Y. Liu, T. P. Chen, Z. Liu, Q. Yu, L. J. Deng, Y. Yin and S. Hosaka, *Appl. Phys. Lett.*, 2013, **103**, 133701.
67 S. Yu, Y. Wu, R. Jeyasingh, D. Kuzum and H. S. P. Wong, *IEEE Trans. Electron Devices*, 2011, **58**, 2729.

Published on 02 April 2021. Downloaded by East China Normal University on 7/6/2021 2:34:28 AM.